

# A Comparative Study of MEMS Microactuators for Use in a Dual-Stage Servo With an Instrumented Suspension

Xinghui Huang, *Member, IEEE*, Roberto Horowitz, *Senior Member, IEEE*, and Yunfeng Li, *Member, IEEE*

**Abstract**—This paper presents the design and analysis of a dual-stage servo system with an instrumented suspension for use in hard disk drives. The dual-stage system is equipped with a microelectromechanical system microactuator (MA), either rotational or translational, as a secondary actuator. In both cases, the MA has a resonance mode at 2.2 kHz and has virtually no other modes up to 40 kHz. Two design approaches, the sensitivity decoupling design and the multiobjective optimization, are applied to the design of the servo system. With either approach, the translational dual-stage actuator achieves better tracking performance than the rotational one by about 13%, which is achieved mainly by attenuating airflow-excited suspension vibrations. This improvement is significant when the servo system's track misregistration (TMR) budget approaches the level of 5–10 nm. The airflow-excited suspension vibrations then become a significant contribution to the TMR.

**Index Terms**—Hard disk drives, microactuators (MAs), servo control, vibration control.

## I. INTRODUCTION

THE increase of data track density in hard disk drives (HDDs) is possible only when the position accuracy of the read/write head can be improved accordingly. For example, at the targeted track density of 500 k tracks per inch (TPI), the allowable track misregistration (TMR) is about 5 nm ( $3\sigma$  value). In order to satisfy higher requirements of position accuracy, it is necessary to develop high-bandwidth, robust track-following servo systems. Dual-stage actuators have thus been proposed and explored intensively as a means of attaining the necessary servo bandwidth to achieve the required compensation of track runout and rejection of various disturbances. In a dual-stage configuration, a secondary actuator is added on to the conventional voice coil motor (VCM) in order to offer better mechanics and faster dynamic responses to compensate for high-frequency disturbances.

Manuscript received April 27, 2005; revised January 5, 2006. Recommended by Technical Editor N. Jalili. This work was supported by the Information Storage Industry Consortium and the Computer Mechanics Laboratory of the University of California at Berkeley.

X. Huang was with the Department of Mechanical Engineering, University of California at Berkeley, Berkeley, CA 94720 USA. He is now with Seagate Research, Pittsburgh, PA 15222 USA (e-mail: xinghui.huang@seagate.com).

R. Horowitz is with the Department of Mechanical Engineering, University of California at Berkeley, Berkeley, CA 94720 USA (e-mail: horowitz@me.berkeley.edu).

Y. Li is with Samsung Information System America, San Jose, CA 95134 USA (e-mail: yunfeng.li@sisa.samsung.com).

Digital Object Identifier 10.1109/TMECH.2006.882982

Although there have been many possible configurations for the secondary actuator, two popular approaches are currently being considered by the disk drive industry and researchers. The first approach is called the actuated suspension type [1], [2], in which a piezoelectric device is placed on the suspension to flex the suspension around a pivot. The second approach is called the actuated slider type [3], [4], in which an electrostatic microelectromechanical system (MEMS) microactuator (MA) is sandwiched between the gimbal and the slider, and it either rotates or translates the slider relative to the suspension tip. The actuated slider approach results in a truly collocated system without exciting the structural resonance modes of the suspension. Besides, the microactuator usually has very clean dynamic responses: it has a single mass-spring mode in the frequency range of 1–3 kHz, and there are no other significant modes up to 40 kHz [4]–[6]. With MEMS fabrication and integration techniques, the MEMS MA can be batch-fabricated and microassembled with the head and gimbal on the suspension. All these features associated with the actuated slider approach provide the potential to develop high-performance servo systems.

There are two types of MEMS MAs: rotational [3] and translational [4], [6]. In the rotational MA case, the actuation of the VCM and MA can be viewed as being decoupled with each other, i.e., each actuator contributes to the head motion independently, resulting in a truly parallel structure. This feature eases the design of servo controllers, especially when the relative motion output of the MA is measurable [7], [8] with embedded capacitive sensors. In the translational MA case, the VCM actuation can excite MA dynamics, resulting in a coupled dual-stage actuator. Any motion at the suspension tip, especially those airflow-induced suspension vibrations, will pass through the mass-spring system of the MA and get filtered before affecting the head motion. This feature is desirable as the allowable TMR approaches  $3\sigma$  5 nm, where airflow-induced suspension vibration becomes a significant contribution to the TMR.

Besides the use of dual-stage actuators for achieving higher servo bandwidth, instrumented suspensions have also been proposed as a means of providing information on airflow-induced suspension vibration [9]–[11]. The sensor output can be used for VCM/suspension mode damping to improve its bandwidth [9], or be used for feedforward vibration compensation [10], or both [11]. This signal can be sampled at a higher rate than that of the position error signal (PES) in order to deal with the high-frequency property of suspension vibrations.

Several controller design methods have been proposed for MEMS-based dual-stage servo systems, which can be roughly

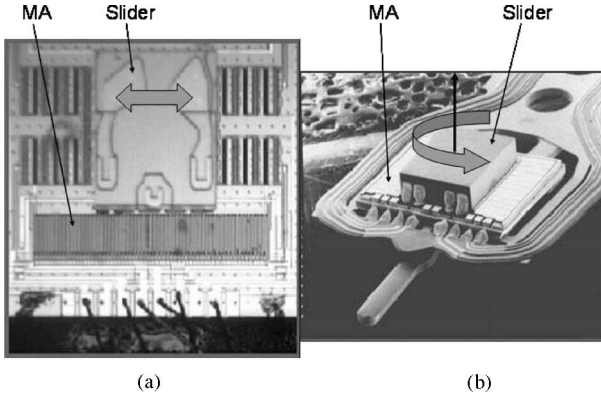


Fig. 1. (a) Berkeley's translational MA (courtesy of K. Oldham). (b) Hitachi Global Storage Technologies' rotational MA (courtesy of M. White).

categorized into two major categories. The first includes those methodologies that utilize sequential single-input single-output (SISO) frequency shaping design techniques, such as the piecewise quadratic method [12] and the sensitivity decoupling method [7], [13]. The second includes those multivariable optimal control design techniques such as  $\mu$ -synthesis [14] and mixed  $H_2/H_\infty$  [11].

This paper presents the design and analysis of a dual-stage servo system with an instrumented suspension. Both rotational and translational MEMS MAs are considered as a secondary actuator. Two design approaches are employed: the sensitivity decoupling approach and the mixed  $H_2/H_\infty$  approach. The difference between rotational and translational MAs and its impact on controller design and system performance are analyzed in detail. Simulation results are presented to verify those observations. This paper is organized as follows. Section II gives a general model for a MEMS MA dual-stage actuator with an instrumented suspension. Detailed controller design is discussed in Sections II–IV, respectively. Section VII gives the simulation results and comparative analysis. Conclusions are provided in Section VIII.

## II. PLANT SETUP AND MODELING

Fig. 1 shows the scanning electron microscopy photograph of a translational and a rotational MA. The mechanisms and block diagram of the two dual-stage actuators are illustrated in Figs. 2 and 3, respectively. The frequency responses of the translational dual-stage actuator are shown in Fig. 4. In these figures,  $u_v$  and  $u_m$  are the control inputs to the VCM and MA, respectively.  $w_a$  is airflow turbulence acting on the suspension, by which suspension resonance modes are excited.  $y_h$ ,  $y_p$ ,  $y_m$ , and  $y_v$  are the read/write head position, the strain sensor output, the relative motion output of the MA, and the suspension tip position, respectively. In conventional disk drive systems, only  $y_h$  is available in the form of the PES when the plant is closed by a tracking controller. In dual-stage actuators with a MEMS MA and an instrumented suspension,  $y_p$  and  $y_m$  are measurable from the strain sensor on the suspension surface and the capacitive sensing embedded in the MA, respectively. In all the cases,  $y_v$  is not measurable.

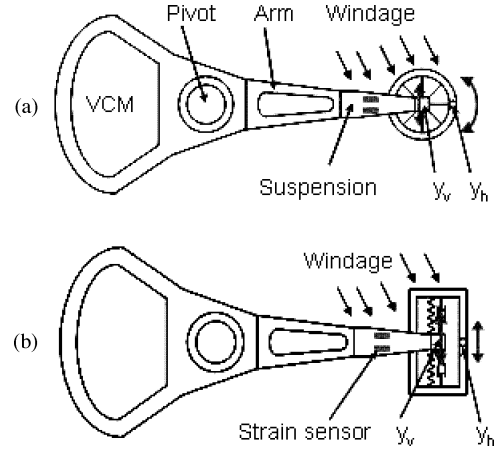


Fig. 2. Mechanisms of translational and rotational MAs.

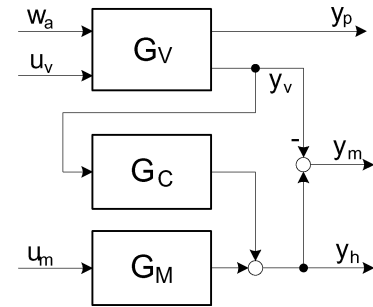


Fig. 3. Block diagram for dual-stage actuators with an instrumented suspension.

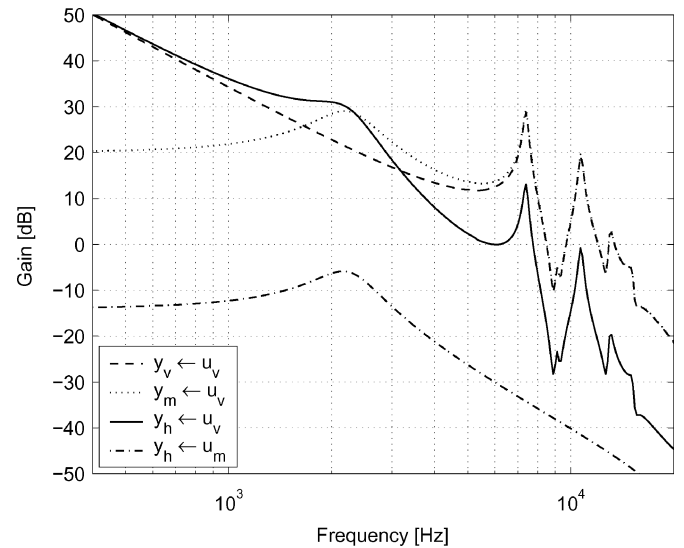


Fig. 4. Frequency responses of the dual-stage actuator.

$G_V$  is the dynamics of the VCM-suspension assembly from  $u_v$  to  $y_v$ , and its transfer function is

$$G_V(s) = \frac{A_0}{s^2} + \sum_{i=1}^N \frac{A_i}{s^2 + 2\zeta_i\omega_i s + \omega_i^2}. \quad (1)$$

In this model,  $G_V$  consists of a rigid body mode, a major sway mode at 7.4 kHz, or called the butterfly mode, and five

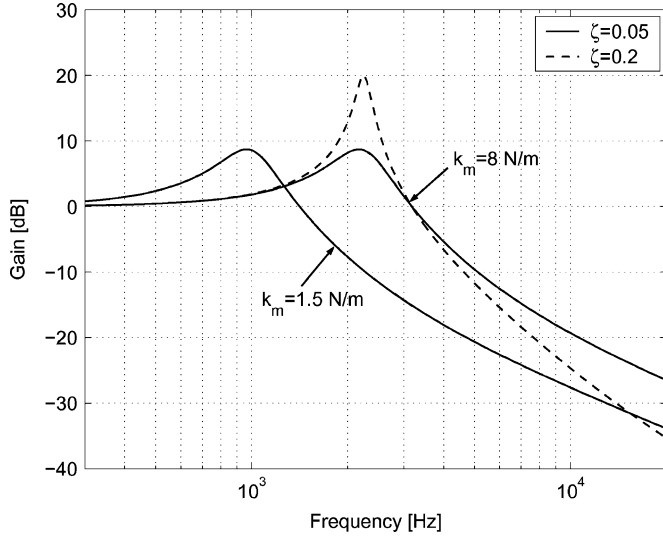


Fig. 5. Frequency responses of the coupling dynamics  $G_C$ .

suspension resonance modes at 5.1, 9.1, 10.7, 13, and 15 kHz, respectively. All these resonance modes have a slight damping coefficient of about 0.015 N·s/m. During operation, high-speed airflow turbulence in the disk drive enclosure acts on the suspension and excites suspension vibrations.  $G_M$  is the dynamics of the MA from  $u_m$  to  $y_h$ , either rotational or translational, and its transfer function is

$$G_M(s) = \frac{A_m}{s^2 + 2\zeta_m\omega_m s + \omega_m^2}. \quad (2)$$

It has been modeled as a single spring–mass–damper system with  $\omega_m = 2.2$  kHz and  $\zeta_m = 0.2$  N·s/m.

$G_C$  is the coupling dynamics from  $y_v$  to  $y_h$ . When the MA is rotational,  $G_C$  is constantly one, then  $y_m$  is solely the output of the MA driven by  $u_m$ , implying virtually no coupling between the VCM and MA [7]. This decoupling effect mainly results from the fact that the translational motion of the suspension tip passes through the MA's center of mass, resulting in no rotational motion of the MA. However, when the MA is translational, we have a coupled dual-stage system.  $G_C$  is then derived from the MA dynamics and can be expressed as

$$G_C(s) = \frac{2\zeta_m\omega_m s + \omega_m^2}{s^2 + 2\zeta_m\omega_m s + \omega_m^2}. \quad (3)$$

This coupling effect implies that actuation of the VCM will excite the dynamics of the MA, and  $y_m$  becomes the combined output of  $u_v$  and  $u_m$ . In both cases, rotational and translational, actuation of the MA can be assumed to have little effect on the VCM dynamics because of the very small inertia of the MA compared to that of the VCM. This assumption implies that the transfer function from  $u_m$  to  $y_p$  is constantly zero.

In the translational MA case, the coupling dynamics exhibit a low-pass filtering effect, as shown in Fig. 5. It can be seen that both the spring stiffness  $k_m$  and the damping coefficient  $c_m$  can affect the filtering effect. This effect makes a difference between the rotational and translational MAs. From the viewpoint of suspension vibration attenuation, we would like to have a soft

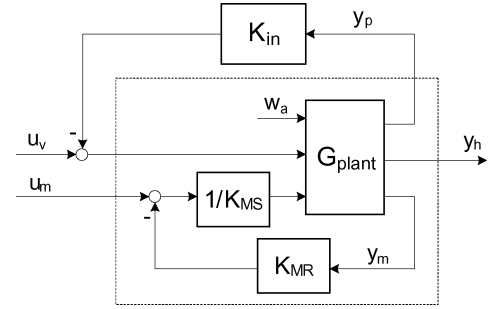


Fig. 6. Minor loop vibration damping and compensation.

spring and a light damping effect, such that most high-frequency suspension vibrations can be attenuated when passing through the MA. However, we want large values for  $k_m$  and  $c_m$  so that the transfer function from  $u_v$  to  $y_h$  has high gains in a wide frequency range for effective track-following control. Therefore, trade off is necessary between vibration attenuation and track following. From Fig. 5, we see that when  $\omega_m = 2.2$  kHz and  $\zeta_m = 0.2$ , the gain of  $G_C$  is above 0 dB up to 3 kHz, implying little degradation of the actuation gain of the VCM-suspension assembly in the low-frequency range for track following, and adequate filtering in the high-frequency range for suspension vibration attenuation.

### III. MINOR LOOP DESIGN OF VIBRATION DAMPING AND COMPENSATION

When  $y_p$  and  $y_m$  are available as auxiliary information, it is possible to first design some minor loop vibration damping controllers before designing an outer loop tracking controller. Besides, the two signals can be sampled at a higher rate than that of the PES so as to achieve better control effects.

#### A. MA Damping Control

The basic use of the relative motion signal  $y_m$  is to actively damp the microactuator resonance mode to make for a well-behaved MA and to simplify the control design that follows. This can be implemented as a minor loop around the MA, as shown in the lower part of Fig. 6. To begin with, the MA plant is first discretized using the zero-order hold at 50 kHz

$$G_M(q^{-1}) = \frac{q^{-1}B_o(q^{-1})}{A_o(q^{-1})} \quad (4)$$

where  $q^{-1}$  is the one-step delay operator. The desired damped MA can be expressed as

$$G_{MD}(q^{-1}) = \frac{q^{-1}B_o(q^{-1})}{A_D(q^{-1})}. \quad (5)$$

This can be achieved by solving the following Diophantine equation

$$A_D(q^{-1}) = A_o(q^{-1})K_{MS}(q^{-1}) + q^{-1}B_o(q^{-1})K_{MR}(q^{-1}). \quad (6)$$

The closed-loop polynomial  $A_D(q^{-1})$  is chosen by the designer and usually the damping coefficient for  $G_{MD}$  is set to be one.

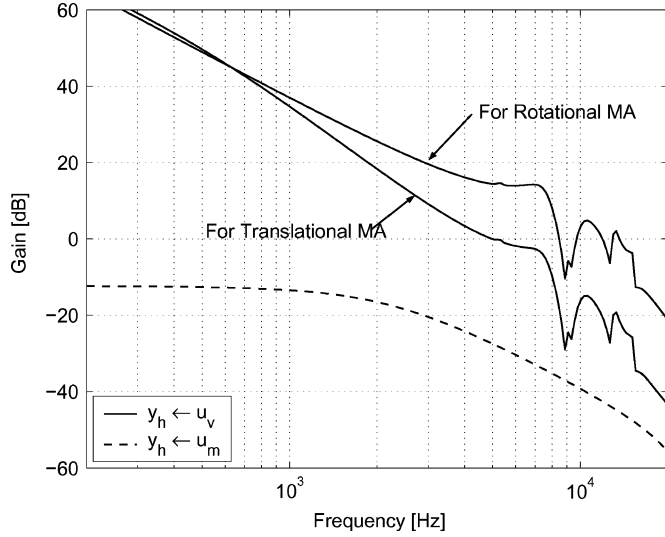


Fig. 7. Frequency responses of the damped plant.

### B. Suspension Vibration Control

After the minor loop around the MA is closed, a vibration controller  $K_{in}$  is designed using  $y_p$  to provide some damping of the suspension resonance modes. The design of  $K_{in}$  is formulated as a standard linear quadratic Gaussian (LQG) problem. Consider the discrete-time representation of the plant with the MA damped, which is shown in the dashed box in Fig. 6

$$\begin{aligned} x(k+1) &= Ax(k) + Bu(k) + B_w w_a(k) \\ y(k) &= Cx(k) + n(k) \end{aligned} \quad (7)$$

where  $y(k) = [y_h(k) y_p(k)]^T$ ,  $u(k)$  is the control input to the VCM, and the airflow turbulence  $w_a(k)$  and measurement noise  $n(k)$  are random signals with zero mean. In this model for controller design, only three major suspension modes are considered in order to restrain the designed controller order. The goal of designing  $K_{in}$  is to minimize the cost function

$$J = E \{ y_h^2(k) + Ru^2(k) \} \quad (8)$$

where  $E\{\cdot\}$  is the expectation operator and  $R$  is the control weighting.

Fig. 7 shows the frequency responses of the two damped plants. Two major resonance modes of the VCM and the MA mode are damped by using  $y_p$  and  $y_m$ , respectively. As evident, the frequency response from  $u_v$  to  $y_h$  for the translational MA case has stronger high-frequency attenuation than that for the rotational MA case due to the coupling effect. This implies that the translational MA will behave better in suspension vibration attenuation that mainly happens in the high-frequency range.

## IV. SENSITIVITY DECOUPLING DESIGN

The decoupling control approach, originally introduced by [13], is popularly applied in the design of track-following controllers for dual-stage servos. This approach utilizes the PES and  $y_m$  to generate the position error of the suspension tip relative

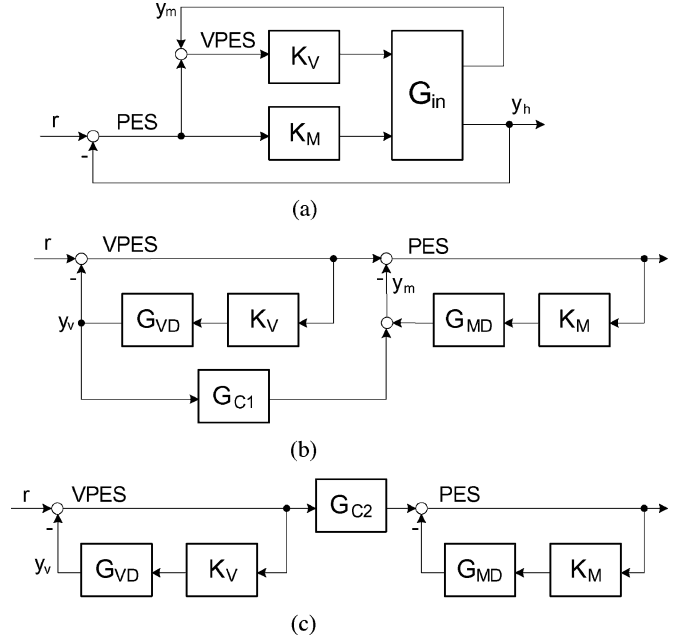


Fig. 8. Block diagram of sensitivity decoupling design.

to the data track center, which will be labelled as VPES

$$VPES = PES + y_m = r - y_v \quad (9)$$

and this signal is then fed to the VCM loop controller  $K_V$ . With this configuration, as shown in Fig. 8(a), the decoupling design of  $K_V$  and  $K_M$  is made possible: the VCM loop and the MA loop can be designed sequentially using conventional SISO design techniques

$$G_{C1} = \frac{K_{MS}}{K_{MS} + G_M K_{MR}} (G_C - 1) \quad (10)$$

$$G_{C2} = 1 - G_{C1} G_V K_V. \quad (11)$$

It is important to pay specific attention to the coupling effect in this design process. The blocks  $G_{C1}$  and  $G_{C2}$  in Fig. 8 are derived from the coupling effect  $G_C$ , as shown in Fig. 3 and (3). As evident, for a rotational MA,  $G_C = 1$ , then  $G_{C1} = 0$  and  $G_{C2} = 1$ , implying exact decoupling between the two minor loops in Fig. 8(c). In the translational MA case,  $G_{C2}$  involves all plant dynamics and controllers designed except for  $K_M$ . The frequency response of  $G_{C2}$  is shown in Fig. 9. It is seen that the dynamics of  $G_{C2}$  is fairly mild: it is about 6 dB in the region 60–500 Hz, and close to 0 dB beyond 1 kHz. Its phase property is mild as well:  $30^\circ$  around 60 Hz and  $-30^\circ$  around 600 Hz. This implies that based on the  $K_M$  designed for the rotational MA case, a modifier which has the similar dynamics to  $G_{C2}$  can be designed to compensate for the coupling effect, yielding a sensitivity response similar to that of the rotational MA case

$$K_{MC} = K_M K_C \approx K_M G_{C2} \quad (12)$$

where  $K_M$  is the controller designed for the rotational MA case,  $K_C$  is the modifier to compensate for  $G_{C2}$ , and its dynamics are also shown in Fig. 9 (dashed lines).

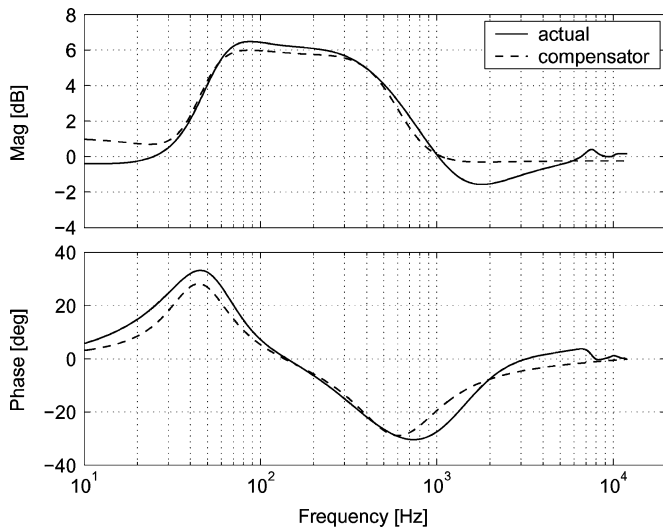


Fig. 9. Frequency responses of  $G_{C2}$  and compensator  $K_C$ .

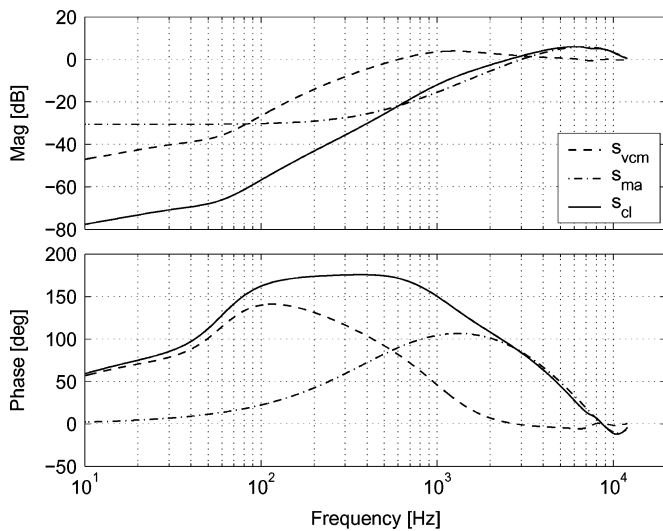


Fig. 10. Sensitivities of the decoupling design with a rotational MA.

In the rotational MA case, the design of  $K_V$  and  $K_M$  is to use pole placement [7]. In this paper,  $K_V$  is designed to achieve a closed-loop bandwidth of 600 Hz for the VCM loop, and  $K_M$  achieves a closed-loop bandwidth of 3 kHz for the MA loop. The final sensitivity is the product of the two and it achieves a closed-loop bandwidth of 2.4 kHz. Their frequency responses are shown in Fig. 10, and the comparison between the designs for rotational and translational MAs is shown in Fig. 11.

## V. MULTI-OBJECTIVE OPTIMIZATION THROUGH LINEAR MATRIX INEQUALITIES (LMIS)

In Section V, a multiobjective optimization method, or called the mixed  $H_2/H_\infty$  approach, is applied to the design of tracking controllers. Unlike the sensitivity decoupling approach, which proceeds sequentially by SISO design methods, the mixed  $H_2/H_\infty$  approach is a MIMO design approach. It formulates the optimization of tracking performance as an  $H_2$  control problem,

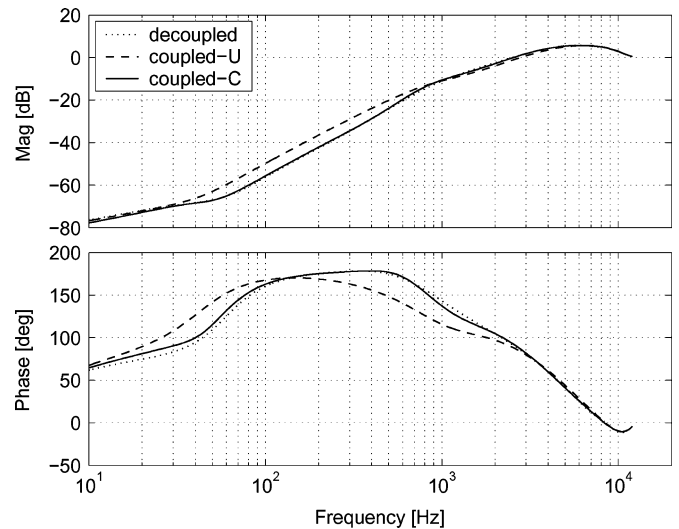


Fig. 11. Comparison of sensitivities for rotational and translational MAs. “decoupled:” original design for the rotational MA case; “coupled-U:” the same controllers applied to the translational MA case without compensation by  $K_C$ ; and “coupled-C:” the system is compensated by  $K_C$ .

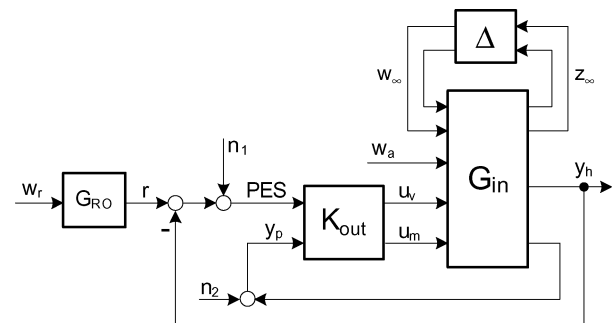


Fig. 12. Block diagram for multiobjective optimization method.

and stability robustness is explicitly considered by posing some  $H_\infty$  norm bounds. Fig. 12 shows the schematic for this method. Its design procedure is briefly explained later [11].

In Fig. 12,  $G_{RO}$  is the frequency shaping function for generating the track runout from the normalized noise  $w_r$ . A third-order function is used to approximate the real signal

$$G_{RO}(s) = \frac{7.8 \times 10^9}{s^2 + 800s + 2.5 \times 10^5} + \frac{1.2 \times 10^5}{s + 1.9 \times 10^3}. \quad (13)$$

The rms value of this runout is about 450 nm in the range of 10 Hz to 25 kHz.  $G_{in}$  is the plant with MA damping and  $K_{in}$  closed, as shown in Fig. 6.  $\Delta_V$  and  $\Delta_M$  are the multiplicative uncertainties of the nominal actuator model

$$\begin{aligned} G_V(s) &= G_{Vnom}(s)(1 + \Delta_V(s)W_V(s)) \\ G_M(s) &= G_{Mnom}(s)(1 + \Delta_M(s)W_M(s)). \end{aligned} \quad (14)$$

Here,  $G_{Vnom}$  and  $G_{Mnom}$  are the nominal dynamics of the VCM and MA respectively,  $\|\Delta_V\|_\infty \leq 1$ ,  $\|\Delta_M\|_\infty \leq 1$ , and  $W_V$  and  $W_M$  are the magnitude bounding functions of the two

uncertainties:

$$W_V(s) = \frac{3s^2 + 3 \times 10^4 s + 1.4 \times 10^8}{s^2 + 4.6 \times 10^4 s + 1.4 \times 10^9}$$

$$W_M(s) = \frac{s + 6.28 \times 10^3}{s + 6.28 \times 10^4}. \quad (15)$$

The first design criterion is expressed so as to minimize the rms value of the PES, or equivalently, the  $H_2$  norm of the transfer function from disturbances to the PES

$$\min \text{rms}(\text{PES}) \Leftrightarrow \min \|G_{z_2 w_2}\|_2 \quad (16)$$

where  $z_2 = [\text{PES} \ u_v \ u_m]^T$  and  $w_2 = [w_r \ w_a \ n_1 \ n_2]^T$ . Stability robustness of the closed-loop system is characterized by the structured singular value [15]

$$\sup_{\omega} \mu_{\Delta}(G_{cl}(j\omega)) < 1 \quad (17)$$

where  $\Delta = \text{diag}[\Delta_V, \Delta_M]$ , and  $G_{cl}$  is the closed-loop plant with  $K_{\text{out}}$  closed around  $G_{\text{in}}$ .

Since the dimension of the  $\Delta$  block is only 2, condition (17) can be approximated by setting  $\mu$ -bounds on the two uncertain channels separately, that is,  $\sup \mu_{\Delta_V}(G_{cl}(j\omega)) < \gamma_V$  and  $\sup \mu_{\Delta_M}(G_{cl}(j\omega)) < \gamma_M$ , with  $\gamma_V$  and  $\gamma_M$  strictly less than 1. They can be further reduced to  $\|G_{\Delta_V}\|_{\infty} < \gamma_V$  and  $\|G_{\Delta_M}\|_{\infty} < \gamma_M$  when  $\Delta_V$  and  $\Delta_M$  are scalars.

From the earlier discussion, we have shown that the multiobjective optimization problem can be cast as an  $H_2$  minimization problem with some  $H_{\infty}$  bounds, i.e., to design an output dynamic feedback controller  $K_{\text{out}}$  such that

$$K_{\text{out}} = \arg \min_{K_{\text{out}}} \gamma_2 \quad (18)$$

$$\text{with} \quad \|G_{z_2 w_2}\|_2 < \gamma_2 \quad (19)$$

$$\|G_{z_{\infty} w_{\infty}, \Delta_V}\|_{\infty} < \gamma_V \quad (20)$$

$$\text{and} \quad \|G_{z_{\infty} w_{\infty}, \Delta_M}\|_{\infty} < \gamma_M. \quad (21)$$

This minimization problem with inequalities can be transformed to a set of LMIs and be solved with some convex optimization algorithm [16].

This approach can be applied to dual-stage servo designs with either a rotational or translational MA, as it is a MIMO design method and does not rely on the specific structure of the plant. As an example, the frequency response of  $K_{\text{out}}$  for the translational MA case, from the PES to  $u_v$ , is shown in Fig. 13. As evident, when  $H_{\infty}$  bounds are imposed, the controller gain in the high-frequency range is reduced significantly compared to the  $H_2$  design in order to achieve more stability margin. The Hankel model reduction technique is then applied to reduce the controller order from 21 to 14 with little dynamic variation.

## VI. ADAPTIVE FEEDFORWARD COMPENSATION FOR SUSPENSION VIBRATION

As mentioned earlier, some suspension resonance modes can be damped by using the strain signal  $y_p$  measured from the suspension surface. This signal can be exploited further to drive the MA to compensate for the airflow-excited suspension vibrations appearing at  $y_h$  [17].

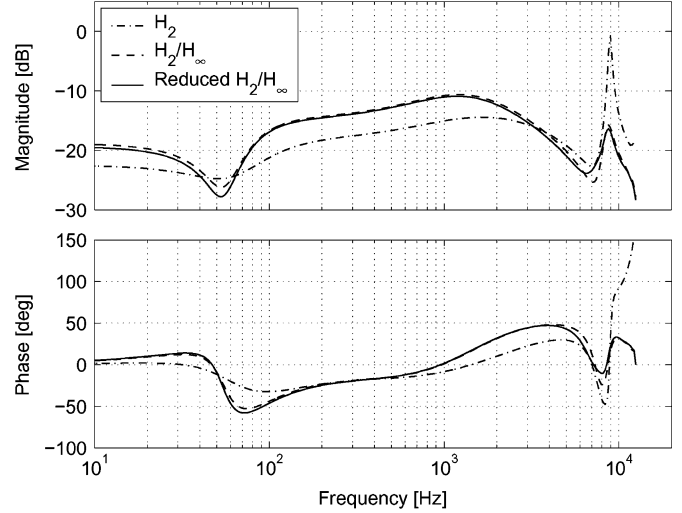


Fig. 13. Bode plots for  $K_{\text{out}}$ .  $H_2$ :  $H_2$  norm minimization only, which is equivalent to the LQG design;  $H_2/H_{\infty}$ : multiobjective design with  $H_{\infty}$  bounds; reduced  $H_2/H_{\infty}$ : reduced-order controller of the second one.

We define  $G_{\text{wp}}$  and  $G_{\text{wh}}$  to be the transfer functions from  $w_a$  to  $y_p$  and  $y_h$ , respectively. We want the feedforward compensator  $K_{\text{MF}}$  to minimize the airflow-excited vibrations at the head, i.e., to minimize

$$e_a = G_M K_{\text{MF}} G_{\text{wp}} w_a + G_{\text{wh}} w_a. \quad (22)$$

This mechanism is different from the feedback damping of the VCM in that the motion generated by the MA cannot directly affect the suspension outputs  $y_v$  and  $y_p$ . Therefore, it can compensate for those vibrations at the head that result from suspension vibration. It is also desirable to tune the coefficients of the feedforward compensator in real time in order to take into account variations in the suspension dynamics and the airflow turbulence characteristics.

In this paper,  $K_{\text{MF}}$  assumes the form of finite impulse response (FIR) for stability consideration:

$$K_{\text{MF}}(\theta, q^{-1}) = h_0 + h_1 q^{-1} + \dots + h_n q^{-n} \quad (23)$$

where  $\theta$  is the filter coefficient vector  $\theta = [h_0 h_1 \dots h_n]^T$  and  $n$  is the order of  $K_{\text{MF}}$ . The feedforward compensation motion can be expressed as

$$\begin{aligned} y_{\text{MF}}(k) &= G_M(q^{-1}) K_{\text{MF}}(q^{-1}) y_p(k) \\ &= K_{\text{MF}}(q^{-1}) G_M(q^{-1}) y_p(k) \\ &= K_{\text{MF}}(q^{-1}) x_f(k) \\ &= \theta^T \phi(k-1) \end{aligned} \quad (24)$$

where  $x_f(k) = G_M(q^{-1}) y_p(k)$ ,  $\phi(k) = [x_f(k) x_f(k-1) \dots x_f(k-n)]^T$ . Since  $x_f(k)$  is not measurable, it is estimated by passing  $y_p(k)$  through the model of the MA,  $\hat{G}_M$ :

$$x_f(k) = \hat{G}_M(q^{-1}) y_p(k). \quad (25)$$

The coefficients of  $\theta$  are tuned in such a manner that  $E\{e_a^2(k)\}$  is minimized. However,  $e_a$  is not directly measurable. Thus, we

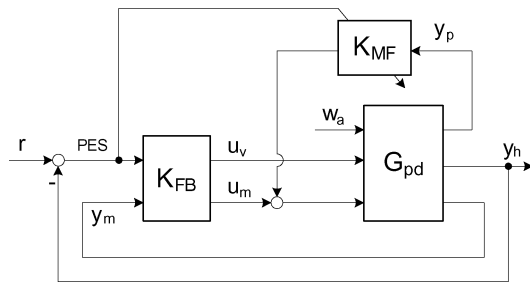


Fig. 14. Block diagram of adaptive feedforward compensation.

have the PES, and it can be written as

$$\text{PES}(k) = e_a(k) + e_r(k) \quad (26)$$

where  $e_r$  represents the tracking error resulting from all other disturbance sources except for the airflow turbulence acting on the suspension. It is roughly valid to assume that  $w_a$  and  $r$  are uncorrelated. Then, we have

$$E\{\text{PES}^2(k)\} = E\{e_a^2(k)\} + E\{e_r^2(k)\}. \quad (27)$$

Thus, minimizing  $E\{e_a^2(k)\}$  is equivalent to minimizing  $E\{\text{PES}^2(k)\}$ , and we can use the PES as a corrupted error signal to perform the adaptation. With  $e_a$  corrupted by  $e_r$ , there will be some degradation in feedforward compensation performance, and a little longer time is expected for the adaptation process to converge.

It is noted that, adaptive feedforward compensation (Fig. 14) does not affect the stability property of the already designed and closed feedback system, since it is an add-on part and aims at minimizing the rms value of the PES by generating additional motion at the MA to compensate for it. Therefore, the vibration compensation part can be implemented on any already-stabilized closed-loop system. It is also expected that feedforward compensation will be more useful in the rotational MA case than in the translational case, since the suspension vibration at  $y_v$  will equally show up at  $y_h$  without any mechanical attenuation. These observations will be verified by the simulation results in Section VII.

## VII. SIMULATION RESULTS

Simulations are conducted to investigate the performance of systems with different structures and controllers. In simulation, the reference signal  $r$  is generated from a combination of various sources, such as repeatable track runout, disk flutter, low-frequency torque disturbances to the VCM, etc. The plant can be either rotational or translational, as illustrated in Fig. 3. To account for parametric uncertainty in the plant, the adaptive feedforward compensator,  $K_{MF}$ , is implemented along with a fixed feedback controller  $K_{FB}$ , which is designed either by sensitivity decoupling or by LMI optimization. Measurement noises are injected into the system at proper locations. The strain sensor signal assumes a signal-to-noise ratio (SNR) of 35 dB. The measurement noise levels of the relative motion of the MA and the PES are 1 nm and 2 nm (rms value), respectively.

Fig. 15 shows the simulation results for various configurations, in which FF means adaptive feedforward compensation of the MA using  $y_p$ . Comparing (a) and (c), we can see significant differences between the rotational and translational MAs, especially in the high-frequency range. There are almost no resonance modes showing up in (c) due to the coupling or filtering effect. Comparing (a) and (b), we see that the LMI design achieves better performance than the decoupling design by optimally shaping the sensitivity function and making a better balance between the attenuation of  $r$  and  $w_a$ . From (c) and (d), we can see more clearly the improvement by optimal shaping.

Table I summarizes the simulation results in more detail. In the table, the total PES has been decomposed into two parts:  $\text{PES}(w_a)$  and  $\text{PES}(r)$ , where  $\text{PES}(w_a)$  is the PES resulting from airflow turbulence, and  $\text{PES}(r)$  contributes the remaining PES resulting from all other disturbance sources including measurement noise. With this decomposition, we can more clearly see the improvement by adaptive feedforward compensation. In the table, R and T denote the rotational and translational plant cases, respectively. Two design methods discussed earlier are employed: the sensitivity decoupling design and the LMI design. Under plant parameter variation, three plant situations are considered: minus, nominal and plus. They indicate how much the plant's modal parameters vary as specified in Table II, where those parameters were defined in (1–3). Those values expressed in percentage indicate the improvement achieved by adaptive feedforward compensation compared to the cases without FF, as shown in the left columns.

Several conclusions can be drawn from Table I.

- 1) The translational MA case always performs better than the rotational MA case in the attenuation of airflow-excited suspension vibrations, no matter what kind of design approach is used. We also see that this improvement is mainly achieved by reducing  $\text{PES}(w_a)$  with little change in  $\text{PES}(r)$ . Obviously this is due to the mechanical or passive filtering effect of the translational MA on suspension vibration.
- 2) The LMI design achieves better performance than the decoupling design by better balancing the attenuation of  $\text{PES}(r)$  and  $\text{PES}(w_a)$ . For the R–N case, both  $\text{PES}(r)$  and  $\text{PES}(w_a)$  are reduced by the LMI design, while for the T–N case, the LMI design reduces  $\text{PES}(r)$  significantly by amplifying  $\text{PES}(w_a)$  a little, resulting in a smaller total PES. This trend can also be seen from Fig. 15. A better balance between  $\text{PES}(r)$  and  $\text{PES}(w_a)$  implies that the final PES becomes closer to a white noise and there is less room for further reduction.
- 3) Adaptive feedforward compensation can further attenuate  $\text{PES}(w_a)$ , especially when there is plant variation. The effectiveness of the feedforward compensation is affected by several factors: the order or the tap number of the compensator  $K_{MF}$ , the sampling rate of  $y_p$ , and the SNR of  $y_p$ . With a higher sampling rate, the compensator will be more effective in dealing with high-frequency resonance modes. During practical implementation, the strain sensor may pick up some resonance modes that do not

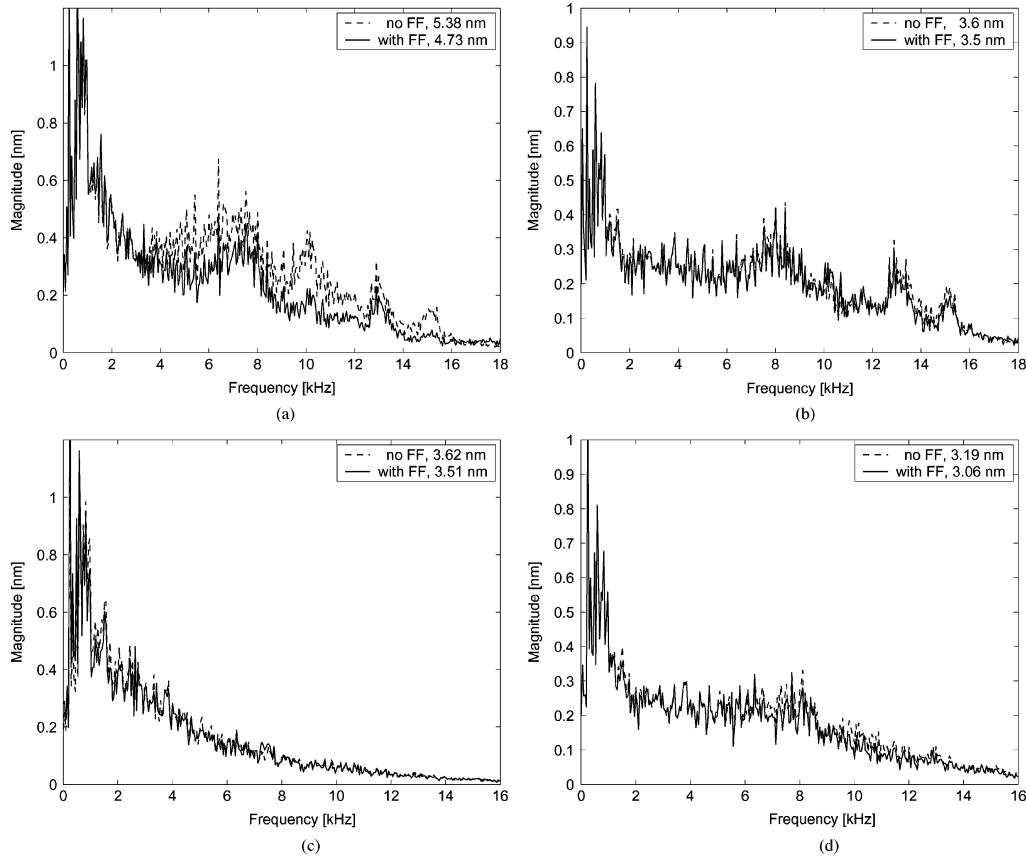


Fig. 15. Power spectra of the PES for various system configurations.

TABLE I  
PERFORMANCE COMPARISON BETWEEN VARIOUS PLANTS AND CONTROL DESIGNS

Plant type	Parameter variation	Tracking controller	PES( <i>r</i> ) [nm]		PES( <i>w<sub>a</sub></i> ) [nm]		total PES [nm]	
			no FF	with FF	no FF	with FF	no FF	with FF
R	N	Decp	3.62	3.57	3.98	3.10 (22%)	5.38	4.73 (12%)
T	N	Decp	3.49	3.51	0.96	0.65 (32%)	3.62	3.57 (2%)
R	M	LMI	2.75	2.73	2.75	2.53 (8%)	3.89	3.72 (5%)
R	N	LMI	2.77	2.74	2.32	2.18 (6%)	3.61	3.50 (3%)
R	P	LMI	2.99	2.93	2.46	2.09 (15%)	3.87	3.60 (7%)
T	M	LMI	2.81	2.82	1.90	1.40 (26%)	3.39	3.15 (7%)
T	N	LMI	2.78	2.78	1.56	1.28 (18%)	3.19	3.06 (4%)
T	P	LMI	2.81	2.79	1.67	1.35 (19%)	3.27	3.10 (5%)

TABLE II  
PARAMETER VARIATIONS OF PLANT RESONANCE MODES

Parameters	Variations		
	Minus	Nominal	Plus
VCM natural frequency ( $\omega_i$ )	-10%	0	+10%
MA natural frequency ( $\omega_m$ )	-15%	0	+15%
Damping coefficient ( $\zeta_i, \zeta_m$ )	-20%	0	+20%
Modal constant ( $A_i, A_m$ )	- 5%	0	+ 5%

contribute to the head offtrack motion. These modes are called nonoff-track modes, and in feed-forward compensation, they just appear as measurement noise to deteriorate the compensation performance. Therefore, optimization in sensor location and orientation is necessary to improve the SNR for better vibration compensation [18].

- 4) The combination of the LMI design and adaptive feedforward compensation can achieve the best performance with fairly good performance robustness. For the rotational MA case, performance degradation under plant variation is less than 6%, while this degradation is less than 3% for the translational MA case. Again, the translational MA case achieves better performance robustness partially due to the coupling-filtering effect, which is very robust to parameter variation.

Some points should be noted on the simulation results. The disturbance model used in the simulation is based on the results from a single-stage system, which may differ from that of a dual-stage system when an MA is added. The MA resonance mode may be excited directly by airflow turbulence. But with the relative MA motion available for inner loop damping, this

effect can be greatly reduced. Sensing noise is also an important issue. The claimed system performance relies on good sensing properties with a high SNR of  $y_m$  [8].

### VIII. CONCLUSION

This paper has explored the difference between rotational and translational MEMS MAs for use in dual-stage servo systems and the resulting effect on the attenuation of airflow-excited suspension vibrations. Due to the inherent coupling effect between the major and secondary actuators for the translational MA case, airflow-excited suspension vibrations can be naturally attenuated, which eases the design of vibration attenuation and servo control. If properly chosen, the resonance frequency of the translational MA can make a good tradeoff between a high gain of  $G_{y_h \leftarrow u_v}$  in the low-frequency range for tracking control, and enough vibration attenuation in the high-frequency range.

Two servo control design approaches have been explored: the sensitivity decoupling design and the mixed  $H_2/H_\infty$  design through LMI. The sensitivity decoupling design yields a set of sequential SISO controllers of low orders that are straightforward to design and implement. In the LMI design, stability robustness is explicitly taken into account by incorporating some  $H_\infty$  bounds with respect to the plant's multiplicative uncertainties.

Simulation results showed that the translational MA is beneficial to vibration attenuation. The LMI design achieves better performance by better balancing the attenuation of  $PES(r)$  and  $PES(w_a)$ . Adaptive feedforward compensation can achieve further attenuation of  $PES(w_a)$  and exhibits good performance robustness under plant variation.

### REFERENCES

- [1] R. Evans, J. Griesbach, and W. Messner, "Piezoelectric microactuator for dual stage control," *IEEE Trans. Magn.*, vol. 35, no. 2, pp. 977–982, Mar. 1999.
- [2] S. Arya, Y.-S. Lee, W.-M. Lu, M. Staudenmann, and M. Hachtett, "Piezo-based milliactuator on a partially etched suspension," *IEEE Trans. Magn.*, vol. 37, no. 2, pp. 934–939, Mar. 2001.
- [3] T. Hirano, M. White, H. Yang, K. Scott, S. Pattanaik, S. Arya, and F.-Y. Huang, "A moving-slider MEMS actuator for high-bandwidth HDD tracking," in *Proc. IEEE Int. Magn. Conf.*, vol. 3, Anaheim, CA, 2003, pp. 2535–2540.
- [4] D. Horsley, N. Wongkomet, R. Horowitz, and A. Pisano, "Precision positioning using a microfabricated electrostatic actuator," *IEEE Trans. Magn.*, vol. 35, no. 2, pp. 993–999, Mar. 1999.
- [5] T. Hirano, L.-S. Fan, W. Lee, J. Hong, W. Imano, S. Pattanaik, S. Chan, R. Horowitz, S. Aggarwal, and D. Horsley, "High-bandwidth high-accuracy rotary microactuators for magnetic disk drive tracking servos," *IEEE/ASME Trans. Mechatronics*, vol. 3, no. 3, pp. 156–165, Sep. 1998.
- [6] K. Oldham, X. Huang, and R. Horowitz, "Design, fabrication, and control of a high-aspect ratio microactuator for vibration suppression in a hard disk drive," presented at the 16th IFAC World Congr., Prague, Czech Republic, Jul. 2005.
- [7] Y. Li and R. Horowitz, "Mechatronics of electrostatic microactuators for computer disk drive dual-stage servo systems," *IEEE/ASME Trans. Mechatronics*, vol. 6, no. 2, pp. 111–121, Jun. 2001.
- [8] M. T. White and T. Hirano, "Use of relative position signal for microactuators in hard disk drives," in *Proc. Amer. Control Conf.*, Denver, CO, Jun. 2003, pp. 2535–2540.
- [9] Y. Huang, M. Banther, P. D. Mathur, and W. Messner, "Design and analysis of a high bandwidth disk drive servo system using an instrumented suspension," *IEEE/ASME Trans. Mechatronics*, vol. 4, no. 2, pp. 196–206, Jun. 1999.
- [10] Y. Li, F. Marcassa, R. Horowitz, R. Oboe, and R. Evans, "Track-following control with active vibration damping of a PZT-actuated suspension dual-stage servo system," in *Proc. Amer. Control Conf.*, Denver, CO, Jun. 2003, pp. 2553–2559.
- [11] X. Huang, R. Nagamune, R. Horowitz, and Y. Li, "Design and analysis of a dual-stage disk drive servo system using an instrumented suspension," in *Proc. Amer. Control Conf.*, Boston, MA, Jun. 2004, pp. 535–540.
- [12] S. J. Schroeck and W. C. Messner, "On controller design for linear time-invariant dual-input single-output systems," in *Proc. Amer. Control Conf.*, San Diego, CA, Jun. 1999, pp. 4122–4126.
- [13] K. Mori, T. Munemoto, H. Otsuki, Y. Yamaguchi, and K. Akagi, "A dual-stage magnetic disk drive actuator using a piezoelectric device for a high track density," *IEEE Trans. Magn.*, vol. 27, no. 6, pp. 5298–5300, Nov. 1991.
- [14] D. Hernandez, S.-S. Park, R. Horowitz, and A. K. Packard, "Dual-stage track-following servo design for hard disk drives," in *Proc. Amer. Control Conf.*, San Diego, CA, Jun. 1999, pp. 4188–4191.
- [15] G. J. Balas, J. C. Doyle, K. Glover, A. Packard, and R. Smith, " $\mu$ -Analysis and synthesis toolbox for use with MATLAB," The MathWorks Inc., Natick, MA, 1995.
- [16] J. F. Sturm, "Using Sedumi 1.05, a MATLAB toolbox for optimization over symmetric cones," The MathWorks, Inc., Natick, MA, 2001.
- [17] Y. Li and R. Horowitz, "Active suspension vibration control with dual-stage actuators in hard disk drives," in *Proc. Amer. Control Conf.*, Arlington, VA, Jun. 2001, pp. 2786–2791.
- [18] CML Blue Report K. Oldham, S. Kon, and R. Horowitz, "Fabrication and optimal strain sensor placement in an instrumented disk drive suspension for vibration suppression," CML Blue Report, Dept. Mech. Eng., Univ. California Berkeley, Berkeley, CA, Tech. Rep. 10, Oct. 2003.



**Xinghui Huang** (S'05–M'06) received the B.S. and M.S. degrees from Tsinghua University, Beijing, China, in 1994 and 1999, respectively, and the Ph.D. degree in mechanical engineering from the University of California at Berkeley, Berkeley, in 2006.

Currently, he is a Research Staff Member with Seagate Research, Pittsburgh, PA. His research interests include vibration control, adaptive control, robust control, multirate control, and mechatronics with applications to disk drive servo and other novel data storage devices.



**Roberto Horowitz** (M'89–SM'02) was born in Caracas, Venezuela, in 1955. He received the B.S. (with honors) and Ph.D. degrees from the University of California at Berkeley, Berkeley, in 1978 and 1983, respectively, both in mechanical engineering.

He is currently a Professor and Vice Chair of Graduate Studies in the Department of Mechanical Engineering, University of California at Berkeley. His current research interests include adaptive learning, nonlinear and optimal control, with applications to microelectromechanical systems, computer disk file systems, robotics, mechatronics, and intelligent vehicle and highway systems.

Dr. Horowitz is a member of the American Society of Mechanical Engineers.

**Yunfeng Li** (S'00–M'03) received the B.S. and M.S. degrees in manufacturing engineering from Beijing University of Aeronautics and Astronautics, Beijing, China, in 1992 and 1995, respectively, and the Ph.D. degree in mechanical engineering from the University of California at Berkeley, Berkeley, in 2003.

He has been a Servo Engineer with Maxtor Corporation, Milpitas, CA. Currently, he is with Samsung Information Systems America, San Jose, CA, where he is engaged in research on disk drive servo control.